The Impact of Stratification on Surface-Intensified Eastward Jets in Turbulent Gyres

LENNARD MILLER[®], a,b Bruno Deremble[®], and Antoine Venaille[®]

^a CNRS, ENS de Lyon, Laboratoire de Physique (UMR CNRS 5672), Lyon, France ^b Université Grenoble Alpes, CNRS, INRAE, IRD, Grenoble-INP, Institut des Géosciences de l'Environnement, Grenoble, France

(Manuscript received 8 November 2024, in final form 11 February 2025, accepted 9 April 2025)

ABSTRACT: This study examines the role of stratification in the formation and persistence of eastward jets (like the Gulf Stream and the Kuroshio). Using a wind-driven, 2-layer quasigeostrophic model in a double-gyre configuration, we construct a phase diagram to classify flow regimes. The parameter space is defined by a criticality parameter ξ , which controls the emergence of baroclinic instability, and the ratio of layer depths δ , which describes the surface intensification of stratification. Eastward jets detaching from the western boundary are observed when $\delta \ll 1$ and $\xi \sim 1$, representing a regime transition from a vortex-dominated western boundary current to a zonostrophic regime characterized by multiple eastward jets. Remarkably, these surface-intensified patterns emerge without considering bottom friction. The emergence of the coherent eastward jet is further addressed with complementary 1.5-layer simulations and explained through both linear stability analysis and turbulence phenomenology. In particular, we show that coherent eastward jets emerge when the western boundary layer is stable and find that the asymmetry in the baroclinic instability of eastward and westward flows plays a central role in the persistence of eastward jets, while contributing to the disintegration of westward jets.

SIGNIFICANCE STATEMENT: Eastward oceanic jets at midlatitudes, such as the Gulf Stream or the Kuroshio, are important in oceanic circulation as they transport water masses from western boundary currents far into the open ocean. To isolate the role of density stratification on the formation of such jets in turbulent gyres, this study uses an idealized model with two layers of fluid stacked on top of each other. Our findings describe layer densities and depths that are favorable for jet formation, highlighting the importance of intensified flow in a thin surface layer.

KEYWORDS: Turbulence; Gyres; Jets; Quasigeostrophic models

1. Introduction

Surface-intensified eastward jets detaching from western boundaries are a prominent feature of midlatitude oceans. Two iconic examples are the Gulf Stream and the Kuroshio, which appear as coherent, narrow, meandering ribbons surrounded by mesoscale oceanic rings in snapshots of surface kinetic energy (Chassignet and Xu 2021). Satellite altimetry and state-estimate reconstructions show that these jets often maintain a coherent structure over long distances, despite the transition from coastal to open-ocean environments (Sánchez-Román et al. 2024; Chassignet and Marshall 2008). Coherent eastward jets are also found across a wide range of models, from high-resolution primitive equation models (Uchida et al. 2022; Ajayi et al. 2020) to highly idealized quasigeostrophic models (Holland 1978; Berloff and McWilliams 1999a). Despite their robust presence in observations and models, the understanding of the turbulent dynamics of eastward jets detaching from the western boundary remains incomplete. Here, we investigate the role of stratification in eastward jet formation using a simple 2-layer quasigeostrophic model of wind-driven ocean gyres.

When a western boundary current detaches, it penetrates into the open ocean as an eastward jet, which tends to become unstable and shed eddies (Veronis 1966; Holland 1978). These eddies can reinforce and sharpen the jet as it flows away from

Corresponding author: Lennard Miller, lennard.miller@ens-lyon.fr

the coast (Wardle and Marshall 2000; Greatbatch et al. 2010; Dritschel and Scott 2011). This has led numerous studies to neglect the connection of the jet to the western boundary current and instead investigate the interaction between turbulence and jets in periodic domains (Arbic and Flierl 2003, 2004; Gallet and Ferrari 2021), where jets may spontaneously emerge due to the planetary vorticity gradient (Rhines 1975). However, it remains unclear how heterogeneity and the presence of a western boundary affect the dynamics of such freely evolving flows (Nadiga and Straub 2010; Grooms et al. 2013). Statistical mechanics may explain the spontaneous emergence of eastward jets in closed domains (Venaille and Bouchet 2011) but fails to account for western intensification. Dynamical system theory can provide insights into the length of a viscous eastward jet detaching from a western boundary current (Simonnet 2005) but is unfit to describe fully turbulent flow. To wit, there is no theoretical framework that can bridge the gap between turbulent eastward jets in the open-ocean and western boundary currents.

In this study, we aim to understand the formation of turbulent jets detaching from western boundaries by characterizing the necessary conditions for their emergence. We focus on the impact of stratification. Previous studies have shown that geostrophic turbulence can reinforce the jet in stratified models of ocean gyres (Sun et al. 2013), while the absence of stratification leads to its complete disintegration (Greatbatch and Nadiga 2000; Fox-Kemper 2005). Two stratification properties are known to influence turbulent flow dynamics in the ocean: the depth of the pycnocline and

the amplitude of the associated density jump. A shallow pycnocline favors surface-intensified dynamics (Fu and Flierl 1980; Smith and Vallis 2001; Meunier et al. 2023). A stronger density jump increases the internal Rossby radius of deformation, a central horizontal length scale of geostrophic turbulence (Vallis 2017). For instance, this length controls turbulent regime transitions from isolated vortices to jets separating regions of homogenized potential vorticity (Arbic and Flierl 2003).

This article further explores the role of stratification by describing its impact on both basin-scale circulation and turbulent eastward jets. For this, we consider a 2-layer quasigeostrophic model of wind-driven ocean gyres which is the minimal model to describe both mesoscale turbulence and Sverdrup gyres. In this model, stratification is also characterized by two key parameters: the layer depth ratio, which translates to the relative depth of the pycnocline, and the internal Rossby radius of deformation. We seek to characterize transitions between flow regimes with and without jets when these two parameters are varied and interpret the results using a combination of linear stability analysis and geostrophic turbulence phenomenology.

The structure of the article is as follows: In section 2, we describe the 2-layer model and introduce the reduced parameter space which describes the vertical stratification properties. In section 3, we use numerical simulations to identify three distinct stratification regimes: strong, intermediate, and weak. We then shift our attention to the intermediate stratification regime. Section 4 presents a local linear stability analysis of surface-intensified gyres, paying particular attention to the distinct stability characteristics of the eastward and westward parts of the gyres, as well as the western boundary layer. In section 5, we compare a 2-layer and a one-and-a-half-layer quasigeostrophic simulation to identify the dynamics specifically linked to baroclinic instability. Finally, in section 6, we discuss the transition to a zonostrophic regime, which precedes the weak stratification regime characterized by barotropic gyres. We conclude in section 7 by outlining the minimal conditions required for the emergence and persistence of a coherent jet between the gyres.

2. Flow model

The simplest model to address the effect of stratification on wind-driven circulation consists of two layers of fluid following quasigeostrophic motion, considered here in a double-gyre configuration. The equations of evolution of the upper-layer and lower-layer potential vorticity $(q_1 \text{ and } q_2)$ are

$$\begin{split} \frac{\partial q_1}{\partial t} + \mathbf{u}_1 \cdot \nabla q_1 &= \frac{\nabla \times \boldsymbol{\tau}}{H_1} + \nu \nabla^4 \psi_1, \ \ q_1 &= \nabla^2 \psi_1 \\ &+ \frac{1 - \delta}{L_d^2} (\psi_2 - \psi_1) + \beta y, \end{split} \tag{1}$$

$$\frac{\partial q_2}{\partial t} + \mathbf{u}_2 \cdot \nabla q_2 = \nu \nabla^4 \psi_2, \quad q_2 = \nabla^2 \psi_2 + \frac{\delta}{L^2} (\psi_1 - \psi_2) + \beta y, \tag{2}$$

where ψ_i is the streamfunction and $\mathbf{u}_i = (u_i, v_i) = (-\partial_y \psi_i, \partial_x \psi_i)$ is the velocity in each layer. We solve this system of equations on a square domain with $(x, y) \in [0, L]^2$. Since our study focuses primarily on regimes with surface-intensified turbulent flow, we consistently neglect linear drag which is often thought to represent bottom friction in the bulk of the domain. We instead choose to dissipate energy along the domain boundary by applying lateral no-slip boundary conditions (Miller et al. 2024).

The forcing $\tau = [\tau_0 \sin(2\pi y/L), 0]$ models a classical double gyre. Stratification is completely described by the relative upper-layer thickness and the first baroclinic Rossby radius of deformation, defined, respectively, as

$$\delta = \frac{H_1}{H_1 + H_2}, L_d = \sqrt{\frac{g' H_1 H_2}{(H_1 + H_2) f_0^2}},$$
 (3)

with H_i being the layer thicknesses, g' being the reduced gravity between both layers, and f_0 being the Coriolis parameter. In addition to δ , the problem admits three nondimensional parameters:

$$\tilde{\nu} = \frac{\nu}{U_{\text{Sv}}L}, \, \tilde{\beta} = \frac{\beta L^2}{U_{\text{Sv}}}, \, \xi = \frac{U_{\text{Sv}}}{\beta L_d^2}, \, \text{with } U_{\text{Sv}} = \frac{8\pi\tau_0}{H_1L\beta},$$
 (4)

 $U_{\rm Sv}$ being the velocity scale of the Sverdrup flow. For all simulations, we set $L=4000~{\rm km}$, $\beta=1.7\times10^{-11}~{\rm m}^{-1}~{\rm s}^{-1}$, $\nu=10~{\rm m}^2~{\rm s}^{-1}$, and $U_{\rm Sv}=0.09~{\rm m}~{\rm s}^{-1}$. The parameters $\tilde{\nu}$ and $\tilde{\beta}$ are thus kept constant at $\tilde{\beta}\simeq3000$, $\tilde{\nu}\simeq10^{-5}$. This corresponds to a thickness of the inertial boundary layer $\delta_I=L/\sqrt{\tilde{\beta}}=72~{\rm km}$ (Charney 1955) and a viscous sublayer of $\delta_P=L\sqrt{\tilde{\nu}/\sqrt{\tilde{\beta}}}=3~{\rm km}$ (Pedlosky 1987; Ierley and Ruehr 1986)

In this study, we focus on the dynamical regimes that appear upon varying the two parameters ξ and δ . The parameter δ is a nondimensional measure of surface intensification of the stratification. In 2-layer models of planetary gyres, δ may be interpreted as the position of the pycnocline and is often placed at $\delta = 0.1$ –0.2 (Flierl 1978). However, as shown in Smith and Vallis (2001), the scenario $\delta \ll 1$ is an interesting asymptotic limit because it corresponds to a situation where barotropization is halted at the first baroclinic mode, contrary to the classical picture where energy cascades to the barotropic mode (Salmon 1998). To investigate this limit, we will consider the range $0.01 \le \delta \le 0.5$ and focus mostly on $\delta = 0.01$. Although this value is probably beyond the realistic value observed in the ocean, the dynamical regimes were easier to entangle for such a small value of δ .

The parameter ξ is the inverse of a nondimensional deformation radius sometimes called the criticality parameter, related to baroclinic instability of the 2-layer model (Stone 1978). We recall here the interpretation of Held and Larichev (1996) and Jansen and Ferrari (2012) adapted to our configuration. Suppose there is a zonal Sverdrup flow of magnitude $U_{\rm Sv}$ confined to the upper layer. The associated potential vorticity gradient in the upper and lower layers is

$$\frac{\partial Q_1}{\partial y} = \beta + \frac{(1-\delta)U_{Sv}}{L_d^2}$$
, and $\frac{\partial Q_2}{\partial y} = \beta - \frac{\delta U_{Sv}}{L_d^2}$. (5)

For baroclinic instability to occur, these gradients have to be of opposite sign (Pedlosky 1987). For westward flow $(U_{\rm Sv} < 0)$, the gradient of the lower layer is always positive, and the condition for baroclinic instability is reached when $\partial Q_1/\partial y < 0$. In the limit $\delta \ll 1$, this corresponds to $\xi > 1$. For eastward flow $(U_{\rm Sv} > 0)$, the gradient of the upper layer is always positive and the condition for instability is given by $\partial Q_2/\partial y < 0$, which corresponds to $\delta \xi > 1$. The criticality ξ therefore serves as a proxy for the baroclinic stability of the large-scale flow, where $\xi < 1$ corresponds to stable flows. Furthermore, there is a second interpretation of ξ in ocean gyres because we can write

$$\xi = \frac{\delta_I^2}{L_d^2}.\tag{6}$$

Then, ξ is a nondimensional measure of the width of the inertial boundary layer relative to the deformation radius.

To reach asymptotic behavior, we vary ξ from 10^{-2} to 10^2 for $\delta = 0.5$, from 1 to 5.6 for $\delta = 1/6$, and from 10^{-1} to 10^3 for $\delta = 0.01$. This corresponds to changing L_d from 737 to 7, 72 to 13, and 233 to 2 km, respectively. In our numerical simulations, we change L_d by setting g', which controls ξ but leaves all other nondimensional variables unchanged. A summary of the dimensional variables of the simulations is given in Table 1

To numerically solve Eqs. (1) and (2), the code qgw was used. It uses classical finite-difference discretization of the equations with an Arakawa formulation of the Jacobian and a direct spectral inversion (after projection on the vertical modes) to obtain the streamfunction ψ from the potential vorticity q. Time stepping is done with an adaptive second-order Adams-Bashforth technique, where the time step is determined by a standard CFL condition. Unless specified, all runs are performed with 4096 \times 4096 grid points on the horizontal, corresponding to a resolution of 1 km, ensuring all relevant flow scales of the problem are well resolved. We paid attention to run the simulations for at least two gyre turnover times $T_{\rm Gyre} = L/U_{\rm Sv}$ after the spinup was completed. Last, the no-slip boundary condition is implemented as in Miller et al. (2024).

3. Numerical simulations

a. Reference run

A reference run displaying an eastward jet detaching from the western boundary is shown in Fig. 1, where the barred quantities denote time averages. The criticality and layer aspect ratio is set to $(\xi, \delta) = (3.3, 0.01)$, corresponding to a deformation radius $L_d = 40$ km. The flow is western and surface intensified in both instantaneous and time-averaged fields, and total transport scales well with the Sverdrup scaling $\psi_{\rm Sv} = U_{\rm Sv} L/4$. The upper-layer potential vorticity is nearly homogenized around values of $\psi_{\rm Sv}/L_d^2$ in each gyre, with the potential vorticity

TABLE 1. Parameters of the 2-layer model for wind-driven oceanic circulation.

-		
Name	Variable	Values in simulations
Upper-layer depth	H_1	2000, 666, 40 m
Lower-layer depth	H_2	2000, 3334, 3960 m
Domain size	L^{-}	4000 km
Beta	β	$1.7 \times 10^{-11} \text{ m}^{-1} \text{ s}^{-1}$
Viscosity	ν	$10 \text{ m}^2 \text{ s}^{-1}$
Deformation radius	L_d	2.3,, 720 km
Wind stress	$ au_0$	$50 \times 10^{-5}, 16 \times 10^{-5},$
		$1 \times 10^{-5} \text{ m}^2 \text{ s}^{-2}$
Sverdrup velocity scale	$U_{ m Sv}$	$0.09 \text{ m}^2 \text{ s}^{-1}$

jump at the interface between the two gyres corresponding to an eastward jet. In instantaneous kinetic energy snapshots, this jet appears with a thickness close to L_d and sheds blobs of potential vorticity that have opposite signs of potential vorticity to the background, similar to Gulf Stream rings (Kurashina et al. 2021). Our aim in this article is to explain how and when stratification renders such states possible in double-gyre configurations without bottom friction.

b. Parameter space

To understand the robustness of eastward jets detaching from western boundaries, we now explore a broader stratification parameter range by spanning the parameter space (ξ , δ), focusing on the asymptotic values of $\delta=0.5$ and $\delta=0.01$. This parameter space, displayed in Fig. 2, is dissected into a strong stratification regime when $\xi<1$, a weak stratification regime when $1/\delta<\xi$, and an intermediate stratification regime in between. As detailed in the next section, the transitions at $\xi=1$ and $\xi=1/\delta$ correspond to the onset of baroclinic instability for westward and eastward flows, respectively. The line $\xi=1/\delta$ also corresponds to the onset of barotropization of the Sverdrup gyres, according to the classical theory of potential vorticity homogenization in planetary gyres (Rhines and Young 1982, see also appendix B). To measure the surface intensification of the large-scale velocity field, we compute the ratio

$$B = \frac{|u_1^{\text{proj}}|}{|u_1^{\text{proj}}| + |u_2^{\text{proj}}|}, \text{ with } u_i^{\text{proj}} = \frac{2}{L^2} \iint \overline{u}_i \cos\left(\frac{2\pi y}{L}\right) dx dy,$$

$$(7)$$

shown in Fig. 3. The projection on the gravest meridional mode is used to remove rectified zonal structures (Fox-Kemper 2004; Nadiga and Straub 2010), and we use the time-averaged zonal velocity \bar{u}_i to weaken the imprint of western boundary currents not accounted for in classical theory (Rhines and Young 1982). The parameter B decreases from 1, corresponding to a complete surface intensification, to 0.5, corresponding to an equality between surface and lower-layer velocities, which we define here as the barotropic state.

In the strong stratification regime (ξ < 1), gyres remain confined to the upper layer, but Gulf Stream–like jets are not observed. Instead, instantaneous fields display strong vortices generated through the detachment of the viscous sublayer at

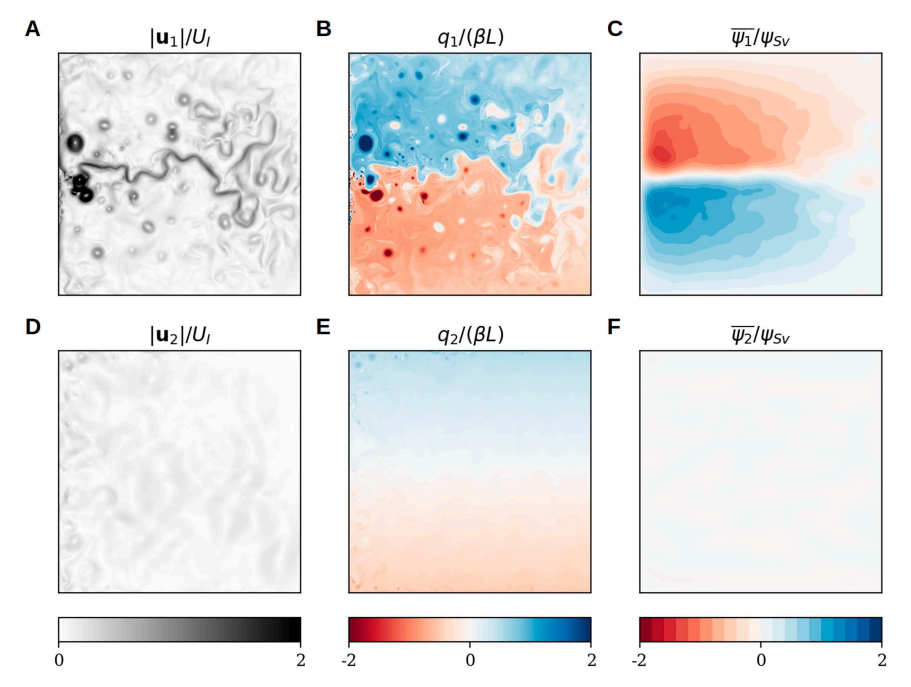


FIG. 1. (top) Upper layer and (bottom) lower layer for the reference run at $\delta = 0.01$, $\xi = 3.3$. (a),(d) Flow speed $|\mathbf{u}_i|$ normalized with inertial velocity $U_I = \psi_{\rm SV} \delta_I$, (b),(e) potential vorticity normalized by planetary vorticity, and (c),(f) time-mean streamfunction normalized by Sverdrup scaling.

the western boundary (not shown). This regime corresponds to "Gyre Turbulence" as reported in Miller et al. (2024), except that the finite value of L_d in the present case tends to stabilize an intense vortex dipole close to the western boundary. The time-averaged bulk structures are similar for both values of δ and resemble a Sverdrup gyre, albeit with notable rectification (Fig. 2, left panels). Although we filter the signal, these rectified barotropic gyres at $\delta = 0.5$ which form close to the meridional boundaries correspond to B less than 1 due to their projection on the gravest meridional mode (Fig. 3a), but in fact, all Sverdrup transport remains confined in the upper layer. We attribute the rectification to the presence of barotropic basin modes which can energize the lower layer when $\delta \sim 1$ (Fig. 3b), but expect a complete decoupling between the two layers in the limit of an infinite Rossby radius of deformation (corresponding to $\xi \to 0$) regardless of the value of δ .

In the weak stratification regime ($\xi > 1/\delta$), the gyres become increasingly barotropic, as measured by B (Fig. 3a). The flow at $\delta = 0.5$ closely resembles the barotropic Gyre Turbulence regime observed by Miller et al. (2024). This barotropization is visible in the collapse of upper- and lower-layer kinetic energies and in the decrease of the index B. For $\delta = 0.01$, the flow enters the weak stratification regime when $\xi > 100$, and the transition is less abrupt than for $\delta = 0.5$. The time-averaged barotropic gyres align more closely with the Sverdrup balance, visible in the decline of B (also in the bottom right panel of Fig. 2). We find large areas of homogenized potential vorticity in the lower layer for both $\delta = 0.5$ and $\delta = 0.01$. However, the upper-layer flow is no longer in Sverdrup balance but instead shows a loss of western intensification. For further

details on the weak stratification regime and potential vorticity homogenization, the reader is referred to appendix B.

The focus of this manuscript lies on the intermediate stratification regime, due to the appearance of eastward jets in gyres such as presented in the reference run. This regime is characterized by $1 < \xi < 1/\delta$ and is hence accessible only when $\delta \ll 1$. We therefore focus on the runs at $\delta = 0.01$, limiting our description to the upper layer as the dynamics remain mostly surface intensified (Fig. 3). The surface flow patterns are displayed in Fig. 4. As ξ is increased, a continuous transition occurs from western-intensified gyres to a state that restores east-west symmetry, with a decrease in total transport of the gyres. Coincidentally, the dominant turbulent flow features change. The strong coherent vortices which dominate the flow in the strong stratification regime disappear, and instead, a sea of eddies of characteristic size L_d develops in the regions of westward flow. In the regions of eastward flow, the transition is marked by the emergence of strong jets, initially as a single jet (1 $\lesssim \xi \lesssim$ 10) and later as multiple jets associated with potential vorticity staircases ($10 \le \xi$).

The runs which were performed at $\delta=1/6$ are omitted in the main text as no eastward jet was observed in this case. Its absence is interpreted as a result of the energetic vortex gas that forms at low viscosity when no-slip boundary conditions are applied (Miller et al. 2024). Further details on these runs can be found in appendix A.

In the remainder of this paper, we use a combination of linear stability analysis, scaling analysis, and complementary simulations to rationalize the transition occurring in the intermediate stratification regime at $\delta = 0.01$ (Fig. 4), rationalizing

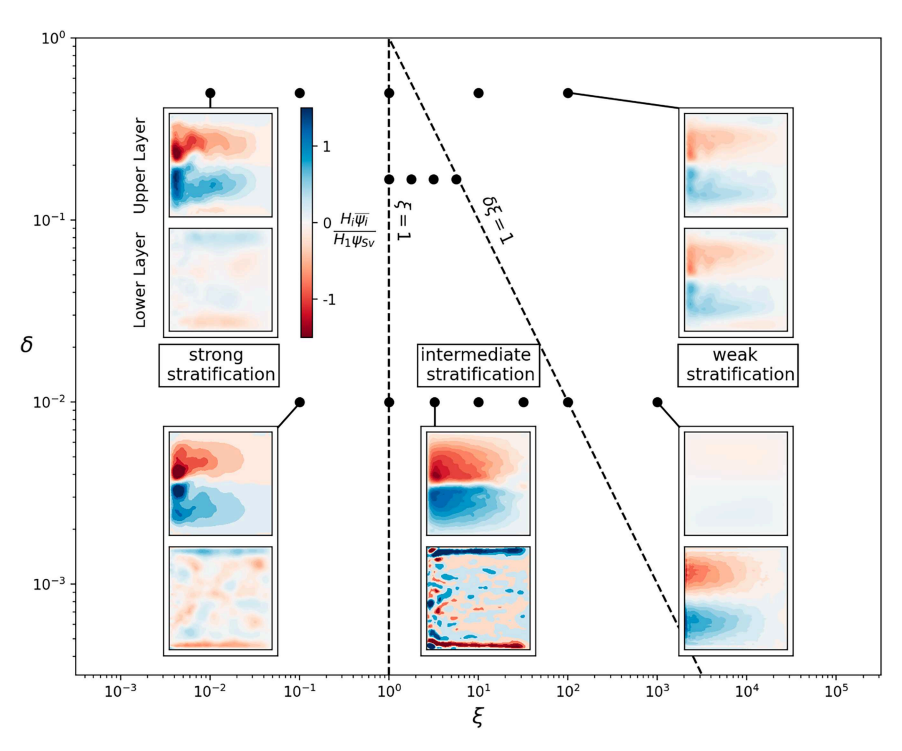


FIG. 2. Parameter space spanned by ξ and δ . The vertical line at $\xi=1$ marks the onset of baroclinic instability, while the slanted line $\delta\xi=1$ signifies the barotropization of a Sverdrup flow. Black dots mark simulation parameters. The inlets show the time-mean vertically integrated transport in the upper and lower layers of runs of each regime. The color scale is normalized by the Sverdrup transport $\psi_{\rm Sv}=U_{\rm Sv}L/4$.

both the emergence and disappearance of the eastward jet detaching from the western boundary.

4. Linear stability analysis

Here, we provide a linear stability analysis of the mean flow associated with surface-intensified gyres and inertial western boundary layers. This analysis will help interpret the parameter space laid out in the previous section. To simplify, we consider two subproblems:

- A horizontally homogeneous eastward or westward flow confined to the upper layer, with prescribed magnitude U_{SV}.
- A meridional velocity profile typical of inertial western boundary currents. This velocity profile varies in the x direction over a scale of δ_I and is invariant in the y direction.

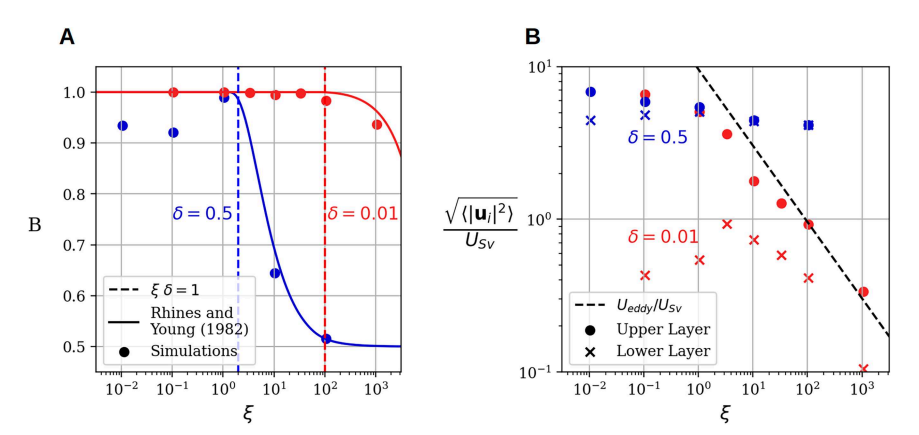


FIG. 3. (a) Barotropization measure B of the mean Sverdrup flow as defined in Eq. (7) and (b) root-mean-square velocity as a function of ξ . For details on the predictions of homogenization theory from Rhines and Young (1982) in (a), the reader is referred to appendix B.

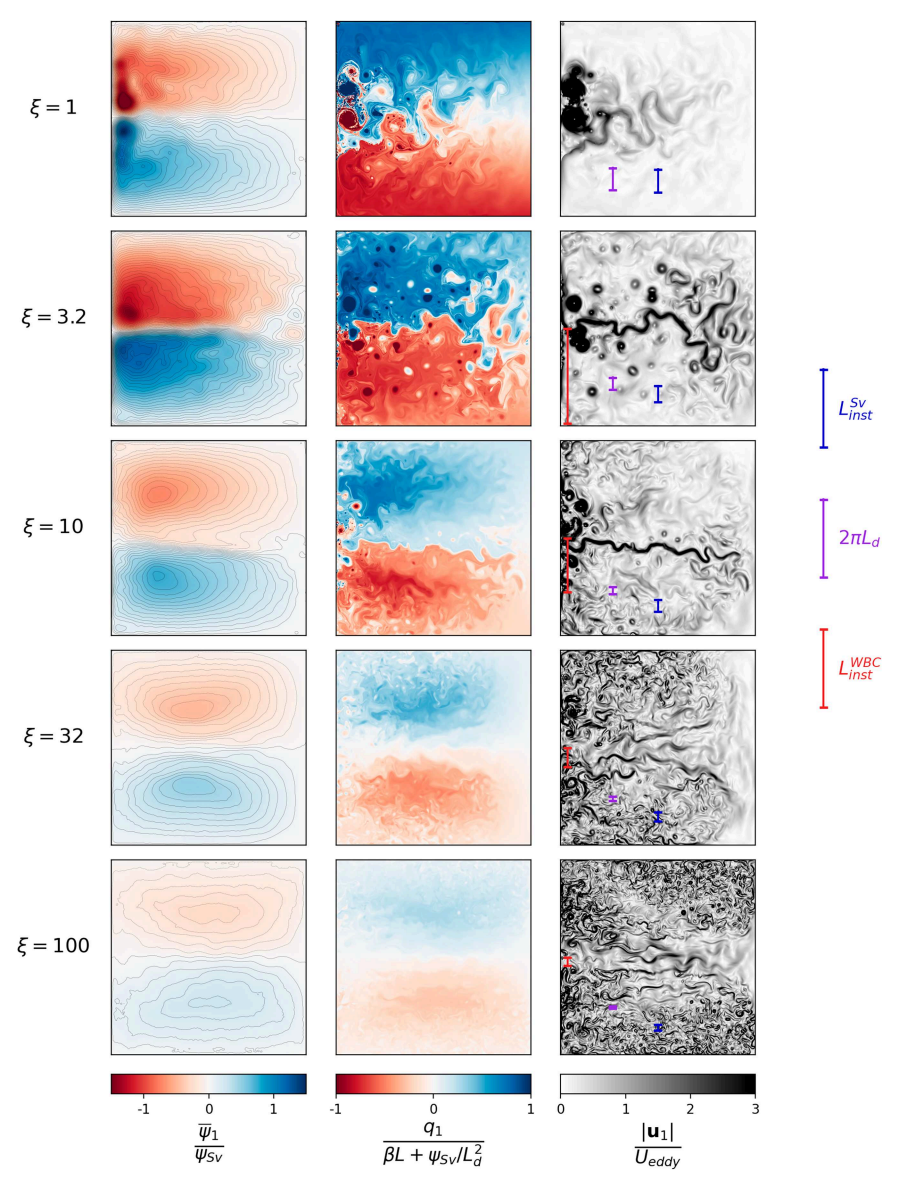


FIG. 4. (left) Time average of ψ_1 and (middle) snapshots of q_1 and (right) $|\mathbf{u}_1|$ for simulations in the intermediate stratification regime at $\delta=0.01$. The streamfunctions are normalized by the Sverdrup scale $\psi_{\rm Sv}$, and contour intervals are 0.05. The q_1 is normalized by the planetary geostrophic vorticity of Sverdrup flow $(\beta L + \psi_{\rm Sv}/L_d^2)$, and the velocity scale $U_{\rm eddy}$ is given in Eq. (10). The brackets shown on the right allow us to compare the instability scales of the western boundary current $L_{\rm inst}^{\rm WBC}$ and of the interior Sverdrup flow $L_{\rm inst}^{\rm Sv}$ to L_d .

The first case is the textbook Phillips problem for baroclinic instability on the beta plane (Vallis 2017). Similar cases to the second one can be found in Ierley and Young (1991) and Berloff and McWilliams (1999b). Here, we present only the key results relevant for interpreting the nonlinear simulations in the parameter space (ξ, δ) . For more details, the reader may consult appendix C.

Baroclinic instability in the Phillips model on the beta plane is known to be asymmetric with respect to the zonal direction of the mean flow (Pedlosky 1987). This asymmetry is illustrated in Fig. 5, which shows the maximum growth rate as a function

of δ and ξ for both eastward and westward Sverdrup flows. The asymmetry appears in the intermediate stratification regime: Westward Sverdrup flow becomes unstable for $\xi > 1$, while eastward Sverdrup flow becomes unstable for $\xi > 1/\delta$. In the weak stratification regime, where surface-intensified flow in both directions is unstable, Sverdrup flow becomes barotropic according to potential vorticity homogenization theory, thus invalidating our initial hypothesis of a surface-intensified gyre.

We also conducted a linear instability analysis of the western boundary layer, as shown in Fig. 6. The base profile of the meridional velocity, depicted in Fig. 6a, is assumed to be

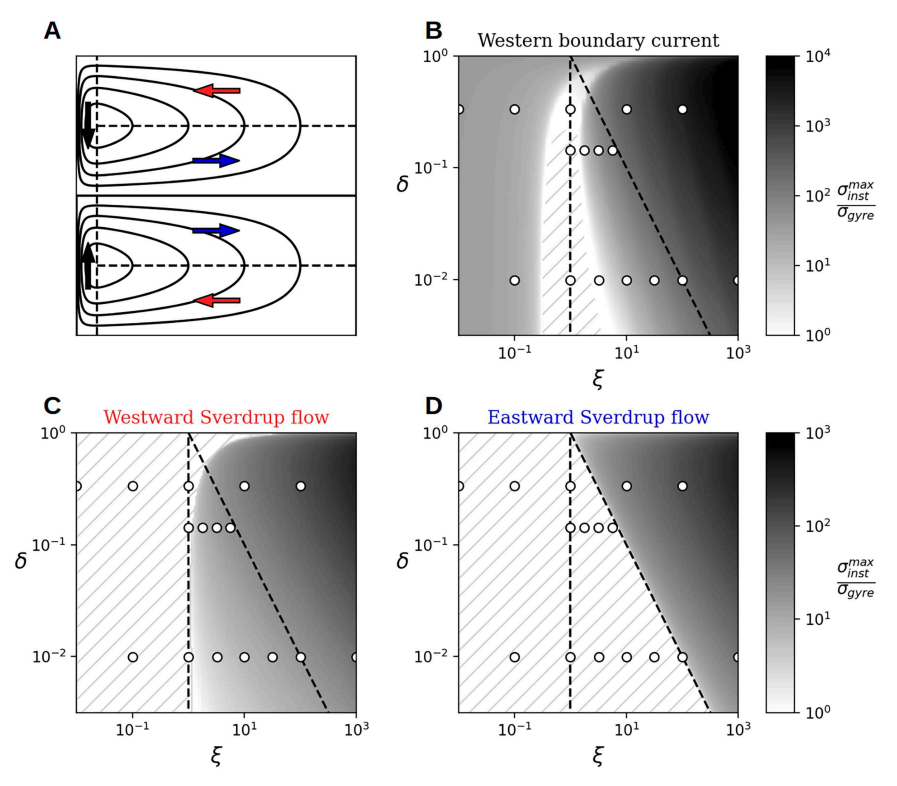


FIG. 5. Results of linear stability analysis of interior Sverdrup flow with an inertial western boundary current. (a) Schematic of the represented regions, and maximum growth rates for (b) western boundary currents, (c) westward Sverdrup flow, and (d) eastward Sverdrup flow. The system is stable in the hatched regions. In the unstable domain, the growth rate (black shading) is rescaled by the gyre turnover rate, $\sigma_{\rm gyre} = U_{\rm Sv}/L$, and the color bar for eastward flow applies for westward flow, too.

$$v = U_I(e^{-x/\delta_I} - e^{-x/\delta_P}). \tag{8}$$

It follows an exponential function with a decay rate determined by the inertial layer thickness δ_I . Additionally, a viscous sublayer is modeled by including another exponential term with a decay rate of δ_P , bringing the velocity to zero near the western boundary. The velocity amplitude is determined by the inertial velocity $U_I = \psi_{\rm Sv}/\delta_I$, ensuring that the gyre's transport fully recirculates within this boundary layer profile. Further details can be found in appendix C. The growth rate of the most unstable mode in this case is plotted as a function of (ξ, δ) in Fig. 5b and in Fig. 6b for the case $\delta = 0.01$. An important result of this analysis is the existence of a stability island around $\xi = 1$ for sufficiently small δ . Near $\xi = 1$, we observe that a meridional flow with characteristic width $\delta_I \simeq L_d$ is stable. This adds to the work of Spall (2000) who showed that a uniform meridional flow is necessarily baroclinically unstable. In Fig. 6b, we also plot the growth rate of the most unstable mode for the same velocity profile in a 1.5-layer quasigeostrophic model, obtained by assuming $\psi_2 = 0$. This demonstrates that instabilities at $\xi < 1$ are due to horizontal shear instabilities of the boundary layer, while instabilities at larger criticality parameters are genuinely baroclinic, as they are absent in the 1.5-layer model.

In Fig. 4 (right panels), we plot the wavelength of the most unstable mode for both the western meridional flow and the zonal Sverdrup flow, to compare this length scale with flow structures. For the Sverdrup flow, the most unstable mode has a length scale $2\pi L_d$, which appears to qualitatively match the size of the vortex rings. In contrast, for the western boundary current, the instability scale is initially much larger than the deformation radius and only at values of $\xi > 10$ approaches the order of the deformation radius. Snapshots of ψ show the presence of large-scale basin modes (not shown), which may result from this instability at intermediate $\xi \sim 10$. At higher $\xi \sim 100$, baroclinic instability is supposedly of the same type as in the Sverdrup flow, as the instability scale becomes much smaller than the scale of the mean profile δ_I . However, at this point, the mean flow is no longer western intensified (Fig. 4a). Baroclinic instability itself may in fact be responsible for this erosion of Sverdrup flow, but a detailed analysis of the mean flow balance is beyond the scope of the present work.

5. The eastward jet (1 $\lesssim \xi \lesssim$ 10): Insights from the 1.5-layer model

To disentangle the role of baroclinic instability and intrinsic surface layer dynamics in the emergence of the eastward jet,

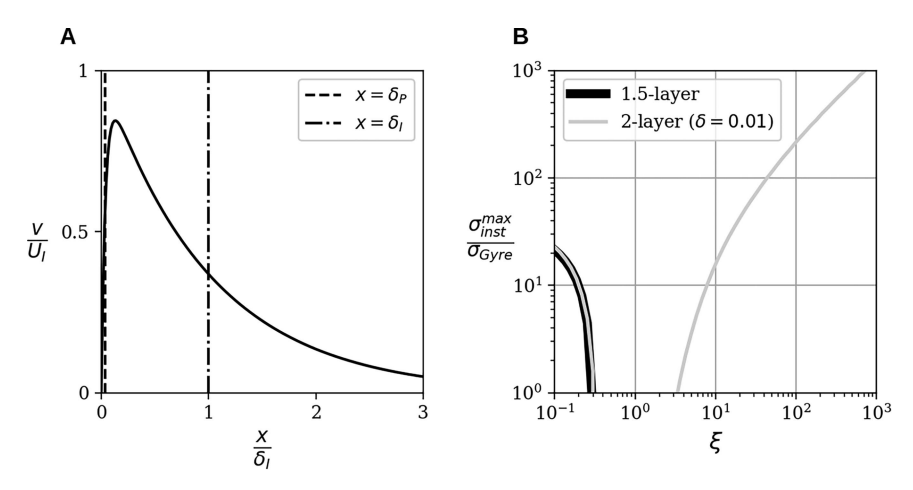


FIG. 6. (a) Base velocity profile for the linear stability analysis of the inertial western boundary layer and (b) comparison of growth rates in the 1.5-layer model and the 2-layer model. The unstable branch at $\xi > 1$ visible in the 2-layer model only is attributed to baroclinic instability.

we performed a set of 1.5-layer numerical simulations, assuming $\psi_2 = 0$ at all times in Eq. (2) with all other parameters kept identical. A comparison between the 2-layer model and the 1.5-layer model is shown with plots of the instantaneous speed in Fig. 7.

In the strong stratification regime ($\xi < 1$), both models yield a similar flow pattern, resembling the Gyre Turbulence regime of Miller et al. (2024). This suggests that the dynamics are primarily governed by 1.5-layer dynamics, consistent with the linear computation predicting no baroclinic instability in this parameter range. As ξ becomes larger than one, both models simulate a change of regime with the emergence of strong eastward jets. However, a notable difference occurs: Recirculating westward jets appear in the 1.5-layer model but not in the 2-layer model (see Figs. 7b,e). We attribute this difference to the zonal asymmetry of baroclinic instability in the intermediate stratification regime. If westward Sverdrup flow is baroclinically unstable, then westward jets will be unstable, too, explaining their disappearance in the 2-layer model. However, we argue that the mechanism for jet creation is the same in both models.

To interpret the emergence of the eastward jet, we focus on the transition observed in the 1.5-layer model and propose two complementary perspectives based on turbulence phenomenology in unbounded geometry and western boundary layer dynamics.

First, we note that the transition from a gas of isolated vortices to jet-like structures is a common occurrence in stratified two-dimensional turbulence (Bouchet and Venaille 2012; Venaille et al. 2015; Frishman et al. 2017). In the specific case of unbounded isotropic 1.5-layer turbulence, it has long been observed that injecting energy at scales much smaller than the Rossby radius of deformation leads to isolated vortices, sometimes organized into vortex crystals (Kukharkin et al. 1995). In contrast, injecting energy at scales larger than the Rossby radius of deformation results in the formation of large-scale potential vorticity staircases (Arbic and Flierl 2003; Burgess and Dritschel 2022). By definition of potential vorticity, the

interfaces of these staircases are associated with sharp jets of width L_d : These are the meandering ribbons, which share strong similarities with the eastward jet detaching from the western boundary. A physical interpretation for the emergence of such potential vorticity staircases has been proposed as the most probable outcome of turbulent potential vorticity mixing (Venaille et al. 2014).

These previous studies suggest that the key parameter governing the transition from a vortex gas to Gulf Stream–like jets is the ratio of the energy injection length scale to the Rossby radius of deformation. In the vortex gas regime, the inertial boundary layer thickness δ_I sets the maximum scale of the eddies injected from the boundary into the bulk, eventually leading to a vortex gas (Miller et al. 2024). This suggests that the transition from a vortex gas to ribbon states is governed by $\delta_I/L_d=\sqrt{\xi}$, which is consistent with the transition occurring at $\xi=1$.

The presence of β and impermeable boundaries in our simulation may change the details of this turbulence-driven transition. We note that isolated vortices drift westward at a speed of βL_d^2 and that the vortex gas regime depends on the ability of these vortices to efficiently interact with the western wall. This interaction is prevented in the eastward parts of the gyres when $U_{\rm Sv} > \beta L_d^2$, which again amounts to $\xi > 1$. Thus, the condition for the existence of the vortex gas regime is also consistent with the observed transition at $\xi = 1$.

So far, we have explained how turbulence may drive a change in the flow pattern within the domain bulk. We now discuss how these patterns may be connected with changes in the western boundary layer dynamics. The emergence of the eastward jet roughly coincides with the stabilization of the western boundary layer (Fig. 5), and we hypothesize this stability to give rise to similar recirculation zones as observed in free-slip solutions (Ierley and Young 1988). Excitation of different inertial recirculation modes, as outlined by Marshall and Marshall (1992), might also be relevant during the transition. In the asymptotic limits, the 1.5-layer solutions are characterized by a pair of contra-rotating vortices near the western boundary when $\xi \ll 1$ (mean flow not shown, but

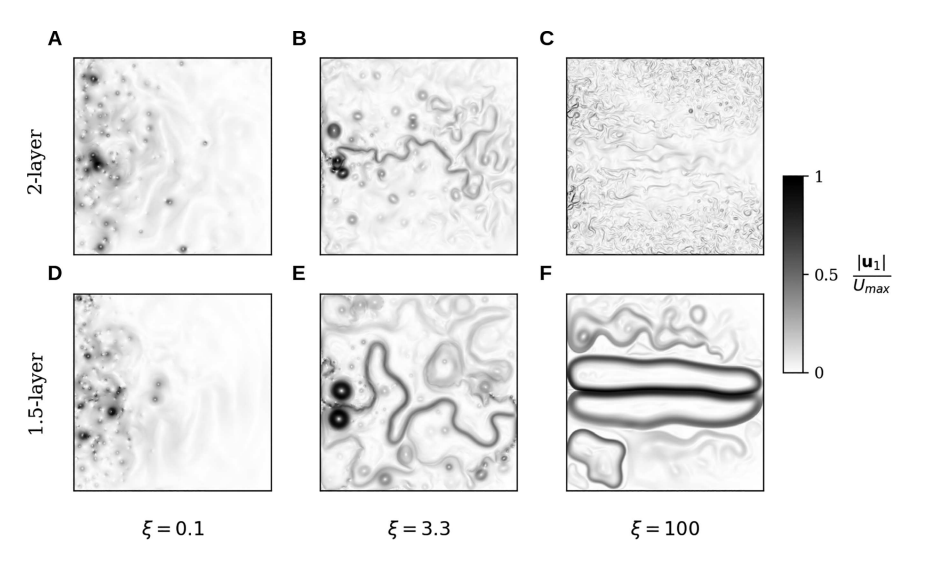


FIG. 7. Comparison of instantaneous surface velocity snapshots between (top) the 2-layer model at $\delta=0.01$ and (bottom) the 1.5-layer model, at (a),(d) $\xi=0.1$, (b),(e) $\xi=3.3$, and (c),(f) $\xi=100$. The maximum velocities in the instantaneous flow fields (renormalized by $U_{\rm Sv}$) for the 2-layer model are 372, 166, and 50, and for the 1.5-layer model, they are 361, 208, and 105. The simulation at $\xi=100$ in the 1.5-layer model is still in the process of spinup.

similar to left panels of Fig. 2) and by Fofonoff flow when $\xi\gg 1$, resembling inertial runaway (Sheremet et al. 1995, Fig. 7f). However, when $\xi\sim 1$, both a strong modon and a penetrating jet are present in the outflow region of the western boundary layer (Fig. 7e), and discussing the flow in terms of stationary inertial solutions only does not seem adequate. Although a mechanism setting the pattern of inertial recirculation is left to be identified, these runs are readily compared to the 2-layer simulations. Intense westward parts of inertial recirculation disappear in the 2-layer runs (Fig. 7b), which is attributed to the zonal asymmetry of baroclinic instability in surface-intensified configurations.

In conclusion, the emergence of a strong eastward jet detaching from the western boundary is driven by the dynamics of the 1.5-layer model, while the 2-layer dynamics are essential for preventing the formation of intense recirculation and westward jets. This is the central result of this paper.

6. The zonostrophic regime (10 \lesssim ξ): Freely decaying turbulence on eastward flow

If ξ is increased further in the intermediate regime, a loss of western intensification occurs and the system enters a zono-strophic regime (Fig. 8). Multiple zonal jets populate regions of eastward flow, and a soup of baroclinic eddies forms in regions of westward flow and close to the western boundary. This regime is likely the same as reported in Nadiga and Straub (2019). In this section, we show that it is best understood as the consequence of strong zonal asymmetry of baroclinic instability.

Following the idea that westward flow produces eddies at scales close to L_d , it is possible to obtain a scaling for the turbulent velocity scale. If the flow is mostly constrained to the upper layer, we obtain a scaling relation by balancing the energy injection

through a Sverdrup interior with dissipation close to a scale L_d . Omitting interactions with the lower layer, the upper-layer energy balance reads

$$\int \frac{\boldsymbol{\tau} \cdot \mathbf{u}_1}{H_1} dA = \nu \int (\nabla^2 \psi)^2 dA, \text{ which scales as}$$

$$\frac{\tau_0 U_{\text{Sv}} L^2}{H_1} \sim \frac{\nu U_{\text{eddy}}^2 L^2}{L_d^2}$$
 (9)

and leads to

$$\frac{U_{\text{eddy}}}{U_{\text{Sv}}} = \frac{C}{\sqrt{\tilde{\nu}\,\xi}},\tag{10}$$

where C is a constant. Figure 3b shows this relation with C = 0.05. The $U_{\rm eddy}$ is thought to describe the eddies observed in the regions of mean westward flow in the zonostrophic regime and fits well with the total average speed (Fig. 3b).

In the region of eastward flow, multiple zonal jets form (Figs. 4 and 8a). In the absence of western intensification, these jets can no longer be considered direct extensions of an overshooting western boundary current as in the previous section, neither can they be the product of a purely local inverse cascade as in Berloff et al. (2009b,a) because of the stability of the background Sverdrup flow. Here, we show that these jets are the result of turbulence, generated through baroclinic instability in the westward-flowing regions, which freely decays in a region of stable eastward flow.

Turbulence on a β plane has a tendency to form zonal jets by creating locally homogenized regions of potential vorticity commonly referred to as staircases (Dritschel and McIntyre 2008) with a spacing of $L^{\rm Rh}=2\pi\sqrt{U_{\rm turb}}\beta$ (Rhines 1975), where $U_{\rm turb}$ is a turbulent velocity scale of the flow. Here, in a 2-layer model with the deeper layer at rest, the surface layer

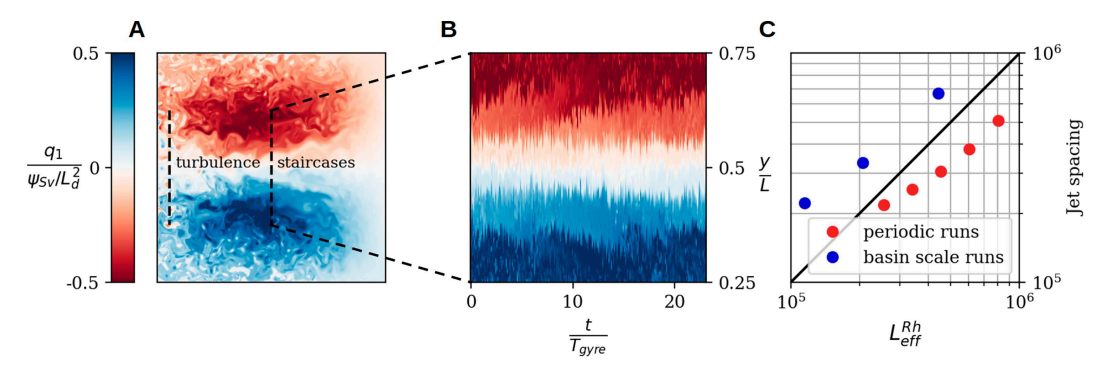


FIG. 8. (a) Snapshot of potential vorticity staircases at $\delta=0.01$, $\xi=33$ with (b) Hovmöller diagram taken at x/L=1/2 and 1/4 < y/L < 3/4. Time is nondimensionalized by the gyre turnover time $T_{\rm Gyre}=L/U_{\rm Sv}$. (c) Comparison of jet scaling with effective Rhines scale $L_{\rm eff}^{\rm Rh}$. The basin-scale runs plotted on this curve are those at $\xi=10,32$, and 100.

dynamics around an eastward mean flow U_m see an effective beta effect $\beta + U_m/L_d^2$ (Burgess and Dritschel 2022). The jet spacing then scales like

$$L_{\text{eff}}^{\text{Rh}} = 2\pi \sqrt{\frac{U_{\text{turb}}}{\beta + \frac{U_{m}}{L_{c}^{2}}}}.$$
 (11)

This formula holds under the assumption of an upper-layer surface-intensified eastward flow, which breaks down when this mean flow is baroclinically unstable. Considering stretching by Sverdrup flow, this occurs in gyres at $\xi=1/\delta$. Therefore, when δ is asymptotically small, there remains a range of criticality parameters $\xi\gg 1$ such that Eq. (11) is valid, with an effective beta term that is dominated by the stretching term induced by eastward Sverdrup flow $(U_m/L_d^2\gg\beta)$.

We argue that this stretching is responsible for the appearance of multiple eastward jets and the creation of potential vorticity staircases in our simulations at $\xi = 10$, 33, and 100. The scaling in Eq. (11) is confirmed in Fig. 8c. Following the idea of nonlocal generation of turbulence, U_{turb} was calculated close to the western boundary and the jet scale and U_m in the bulk (Fig. 8a, "turbulence" and "staircases," respectively). To further support the enhanced stretching on an imposed background flow, the scarce data available from the basin-scale runs were complemented with periodic simulations of decaying surface-intensified turbulence with an imposed background flow. Although slightly offset, they also follow the jet spacing given by Eq. (11). For further details on the periodic runs, extraction of U_{turb} , U_m , and the jet scale, the reader may consult appendix D.

Replacing the scaling for $U_{\rm turb}$ by $U_{\rm eddy}$ and U_m by $U_{\rm Sv}$ in Eq. (11), it is possible to predict the onset of the zonostrophic regime by equating $L_{\rm Rh}^{\rm eff}$ and the size of the region of eastward flow, L/2. Although the result depends on a number of constants in front of the scaling relations, simply inserting $U_{\rm eddy}$ as shown in Fig. 3b into Eq. (11) yields a predicted regime change at $\xi \approx 9$, consistent with numerical experiments. At higher criticality, a precise prediction of the jet scale fails, arguably due to the difference between local and global values of root-mean-square velocity and an incorrect stretching due to the departure from Sverdrup flow at large scales.

In summary, the zonostrophic regime is a result of the strong asymmetry of baroclinic instability in the limit of small δ . Sverdrup theory and classic descriptions of western boundary currents no longer match the observed flow, even on a qualitative level. Instead, a clear separation of scales between mean flow heterogeneity and the size of the turbulent structures appears, and the regime is well understood in the framework of unbounded turbulence on an effective β plane.

7. Discussion and conclusions

We found that stratification properties play a crucial role in the emergence of surface-intensified eastward jets in 2-layer quasigeostrophic models without bottom friction. The important nondimensional numbers in this context are the criticality parameter ξ , which decreases with the density difference between layers, and δ , the ratio of the depths of the two layers.

When the criticality parameter is smaller than one, turbulence takes the form of a western-intensified vortex gas. An energetic eastward jet at the intergyre boundary only emerges when ξ is roughly between 1 and 10. As the criticality parameter increases further, the flow enters a zonostrophic regime, with multiple jets filling the eastward part of the gyres and baroclinic eddies occupying the westward part. Eventually, when $\xi > 1/\delta$, the flow starts to become barotropic.

The emergence of the eastward jet detaching from the western boundary when $\xi > 1$ can be understood from two perspectives. First, linear stability analysis indicates that the jet's formation coincides with the stabilization of the inertial western boundary layer, suggesting an interpretation of the westward jet as an overshooting boundary layer. Second, the observed transition from a vortex gas to eastward jets also occurs in unbounded 1.5-layer dynamics when the energy injection length scale exceeds the Rossby radius of deformation L_d . Here, we argue that both mechanisms, albeit of different nature, are active in the 2-layer model of wind-driven circulation when $\xi \sim 1$.

In the 1.5-layer model, the eastward jet emerges similarly to the 2-layer case when ξ increases above one. However, this process also leads to westward jets, which are not present in the 2-layer model. We showed that these westward jets are

disintegrated by baroclinic instability, explaining the establishment of the western boundary current extension as a single eastward jet.

In this study, we investigated values of δ smaller than the usual oceanic configuration, but the flow dynamics at small δ remain relevant for understanding the classical configuration. Despite the asymptotically small value of δ , the flow of the reference case shares many properties with the flow obtained with $\delta \sim 0.2$, free-slip boundary conditions, and bottom friction (Holland 1978) (see also appendix A). The underlying dynamical similarity between the classical flow configuration and the regime at $\delta = 0.01$ becomes apparent in the results of linear stability analysis. Both configurations feature unstable westward Sverdrup flow, but eastward Sverdrup flow and inertial boundary currents are stable. Less extreme surface intensification will likely shift the exact location of the eastward jet in the parameter space of a more realistic model. If understood as the transitory state between a vortex gas and a zonostrophic regime (Fig. 4), its formation may be altered, for example, by bottom friction (Held and Larichev 1996; Gallet and Ferrari 2021) or topographic stretching close to the western boundary (Boland et al. 2012).

A common concern with quasigeostrophic models of ocean gyres is how sensitive they are to boundary conditions. While free-slip boundary conditions tend to produce more intense eastward jets (Haidvogel et al. 1992; Deremble et al. 2011; Nasser et al. 2023), we showed that jets still form in a no-slip configuration if the stratification is appropriately chosen. One reason for this insensitivity to boundary conditions observed here might be the stability of the inertial western boundary layer in the 2-layer system (Fig. 5), which is easier to model with free-slip boundary conditions (Ierley and Young 1991).

The main result of this article is that in a baroclinic model, the gyre pattern and the eastward jet are primarily shaped by stratification. This contrasts with the strong dependence of the structure of turbulent baroptropic gyres on dissipative processes (Fox-Kemper and Pedlosky 2004). To support the lesser role of dissipation in baroclinic configurations, we note the striking similarity between the free-slip, bottom friction run (Fig. A1) and the no-slip, no bottom friction run (Fig. 1), and emphasize that bottom friction is not required to rationalize the emergence of the jet. However, an efficient dissipation mechanism is required to prevent the formation of an energetic vortex gas that may disrupt jet formation (appendix A). Of course, these energetic flows violate quasigeostrophic assumptions (Scott and Straub 1998) and are prone to ageostrophic energy sinks (Dewar and Hogg 2010; Nikurashin et al. 2013; Brüggemann and Eden 2015), which, besides bottom friction, will likely become important for dissipating eddies in more realistic scenarios.

We conclude that the minimal ingredients for the emergence of a coherent eastward jet extending from western boundary layers in turbulent quasigeostrophic gyres are (i) a criticality parameter ξ that is sufficiently large to permit baroclinic instability ($\xi > 1$) but sufficiently small to leave surface-intensified Sverdrup flow intact ($\xi < 1/\delta$), (ii) a layer depth aspect ratio δ sufficiently small for baroclinic instability to exhibit zonal asymmetry but release energy toward eddies in adjacent areas

of westward recirculation, and (iii) an efficient energy sink which suppresses unrealistic eddy-driven flows.

A natural extension of the present work is to use these findings to understand the dynamical regimes observed in the World Ocean. The first step will be to go beyond the quasi-geostrophic model, which assumes a prescribed, horizontally homogeneous stratification profile. The second step will be to generalize the results obtained from a 2-layer model to continuously stratified models. We are currently investigating these two issues using both climatological data and primitive equations model runs.

Acknowledgments. This project has received financial support from the CNRS through the 80 Prime program and was also partially funded by the French Agence Nationale de la Recherche (ANR), under the projects ANR-23-CE01-0009 and ANR-23-EXMA-0003. The numerical simulations were performed using HPC resources at PSMN Lyon and GENCI HPC (allocation A0150112020).

Data availability statement. Data used in this article were produced with the code qgw (https://doi.org/10.5281/zenodo. 13990523). Python notebooks for the calculation of potential vorticity homogenization and linear stability analysis are available online (https://doi.org/10.5281/zenodo.14055345). Please contact the corresponding author for access to simulation data.

APPENDIX A

Comparison to Realistic Values of δ

A more traditional approach to modeling energy dissipation in quasigeostrophic wind-driven gyres is to apply free-slip boundary conditions and model bottom friction via the inclusion of a linear drag term of the form $-r\nabla^2\psi_2$ on the right-hand side of the equation for the bottom layer in Eq. (2) (Holland 1978). A standard run, at $\delta=1/6$, is shown in Fig. A1, sharing many of the properties listed for the reference run: western and surface intensification, homogenization of potential vorticity inside the gyres, and the presence of a strong eastward jet at the interface between the homogenized potential vorticity pools.

The jet also disappears in this configuration when entering the regimes of strong and weak stratification regimes in this configuration, as illustrated in Fig. A2. Strong vortices appear close to the western boundary current as in the no-slip configuration where energy is dissipated by vorticity filaments. In the strong stratification regime, the flow is completely confined to the upper layer, while in the weak stratification regime, the flow becomes completely barotropic. The flow dynamics of these regimes are investigated in Greatbatch and Nadiga (2000).

If bottom friction is replaced by a no-slip boundary condition as an energy sink, an energetic vortex gas was observed instead of the jet at $\xi=1$, $\delta=1/6$ (Fig. A3). Jet solutions emerged under three conditions: (i) the addition of bottom friction, (ii) an increase in viscosity, or (iii) a decrease in the layer depth aspect ratio. Its reappearance at

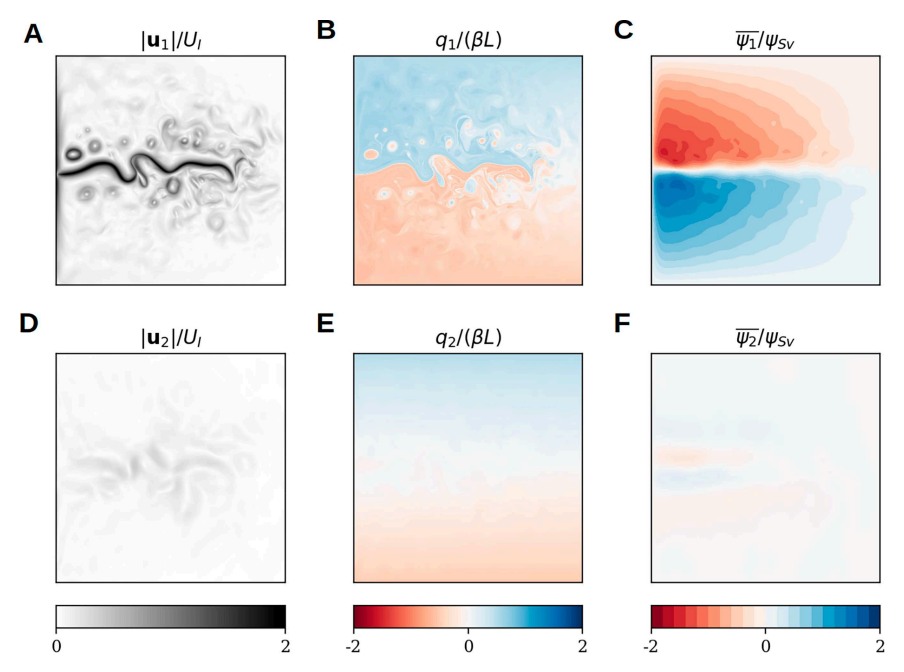


FIG. A1. (a),(d) Flow speed, (b),(e) potential vorticity, and (c),(f) mean streamfunction of a simulations at $\delta=1/6$ ($H_1=666$ m, $H_2=3334$), $\xi=1.3$, with free-slip boundary condition and a drag coefficient $r=3.3\times10^{-7}$ s⁻¹. Note the similarity between this regime and the reference run presented in Fig. 1.

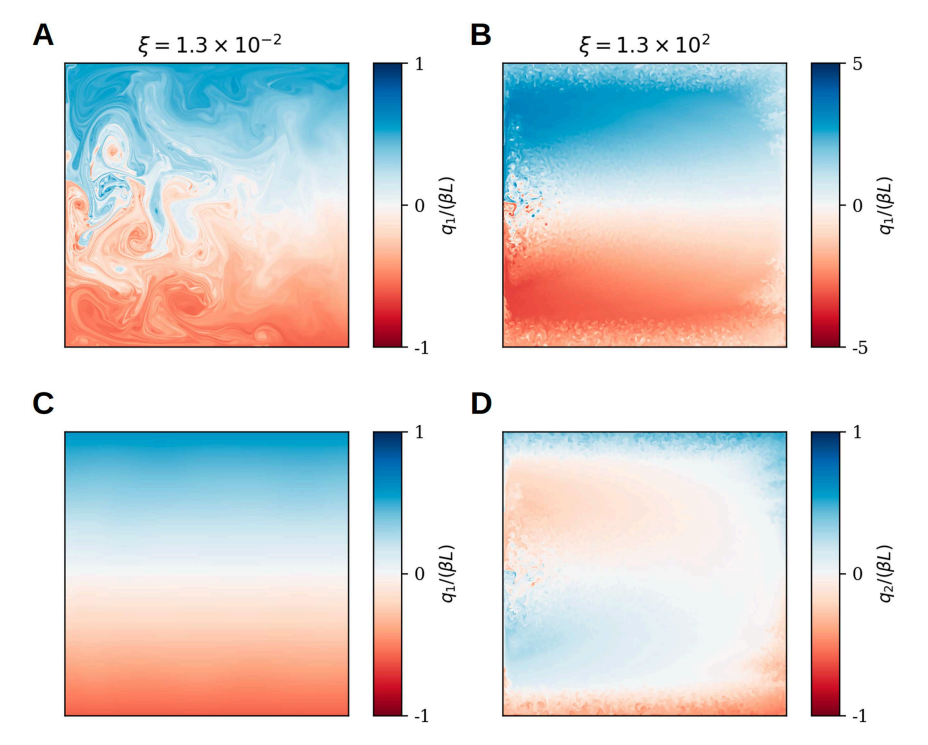


FIG. A2. Snapshots of (a),(b) upper-layer and (c),(d) lower-layer potential vorticity of the free-slip, bottom friction configuration as in Fig. A1 but in the strong ($\xi=1.3\times10^{-2}$) and weak ($\xi=1.3\times10^{2}$) stratification regime. In both regimes, the jet disappears and is replaced by energetic vortices close to the western boundary.

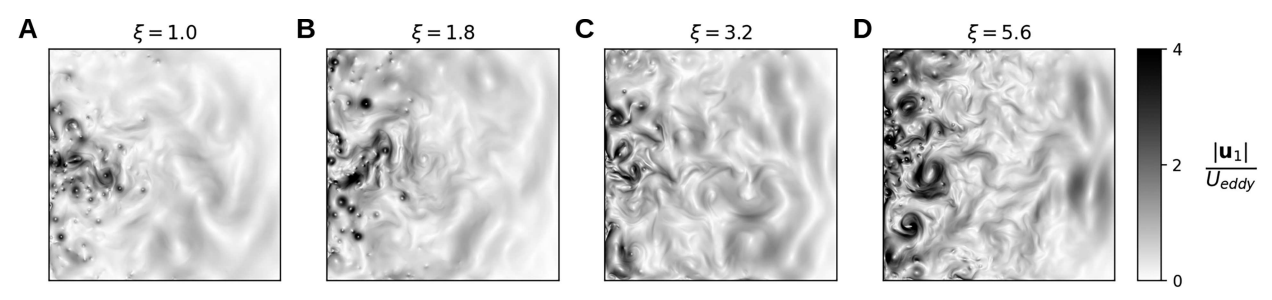


FIG. A3. The upper-layer flow speed of runs without bottom friction at $\delta = 1/6$ ($H_1 = 666$ m, $H_2 = 3334$ m) for (a) $\xi = 1$, (b) $\xi = 1.8$, (c) $\xi = 3.2$, and (d) $\xi = 5.6$. Note the absence of jets.

lower $\delta=0.01$, presented as the reference run in the main text, may be understood as the consequence of the stability island of the western boundary layer becoming larger as δ is decreased (Fig. 5). An inertial overshoot of the western boundary layer remains possible at smaller values of L_d , where smaller vortices dissipate energy more effectively [Eq. (10)]. These vortices thus become less energetic, and the jet may support their presence.

APPENDIX B

Details on the Regime of Weak Stratification

a. Potential vorticity homogenization theory

Calculations on potential vorticity homogenization in 2-layer oceanic gyres can be found in classical textbooks (Vallis 2017). A simple extension including unequal layer depths is given here, with a focus on the mechanism responsible for the onset of homogenization in the lower layer. We write the quasigeostrophic equations on a modal basis, neglecting time derivatives and relative vorticity contributions, but including diffusion of potential vorticity instead of relative vorticity:

$$\beta \frac{\partial \psi_{\rm bt}}{\partial x} = \frac{\nabla \times \tau}{H_1 + H_2}, \ \psi_{\rm bt} = \frac{H_1 \psi_1 + H_2 \psi_2}{H_1 + H_2}, \tag{B1}$$

$$\beta \frac{\partial \psi_{\rm bc}}{\partial x} - \frac{1}{L_d^2} J(\psi_{\rm bt}, \, \psi_{\rm bc}) = \frac{\nabla \times \boldsymbol{\tau}}{H_1} + \nu \frac{\nabla^2 \psi_{\rm bc}}{L_d^2}, \, \psi_{\rm bc} = \psi_1 - \psi_2. \tag{B2}$$

When L_d is large, the advective term for the baroclinic mode can be neglected, and all transport happens in the upper layer. A change in regime occurs when the advective term of the baroclinic mode starts to be on the same order of magnitude as the β term. Using Sverdrup scalings for $\psi_{bc/bt}$ as obtained from Eqs. (B1) and (B2), this occurs when

$$1 \sim \frac{\frac{1}{L_d^2} J(\psi_{\rm bt}, \psi_{\rm bc})}{\beta \frac{\partial \psi_{\rm bc}}{\partial r}} \sim \frac{U_{\rm Sv} H_1}{\beta L_d^2 (H_1 + H_2)} \sim \delta \xi. \tag{B3}$$

Baroclinic instability is not required for this change to occur, and it is only the baroclinic/barotropic advection that alters the dynamical balance of the Sverdrup flow.

However, baroclinic instability will always be present at the onset of inertial recirculation in surface-intensified flows, its sole effect being represented by the presence of weak diffusion of potential vorticity. This diffusion sets the final flow by homogenizing potential vorticity in the lower layer. The solution is then given by matching the contours at the center latitude y = L/2 and separating regions of blocked and closed geostrophic contours. The solution is written in terms of

$$\overline{\psi} = \frac{2\pi\tau_0}{\beta(H_1 + H_2)} \sin\left(\frac{2\pi y}{L}\right) \left(1 - \frac{x}{L}\right), \tag{B4}$$

$$\overline{q} = \beta y + \frac{\overline{\psi}}{L_d^2}.$$
 (B5)

Geostrophic contours are blocked in the northern gyre if $\overline{q} > \beta L/2$ and in the southern gyre if $\overline{q} < \beta L/2$. The upper-layer solution is then given by

$$\psi_1 = \frac{(H_1 + H_2)\overline{\psi}}{H_1}.$$
 (B6)

Else, for a closed contour, homogenization of potential vorticity in the lower layer leads to

$$\psi_1 = \overline{\psi} - \frac{H_1}{H_2} \beta L_d^2 \left(y - \frac{L}{2} \right). \tag{B7}$$

The lower-layer $\psi_2 = [(H_1 + H_2)\overline{\psi} - H_1\psi_1]/H_2$ carries the remaining transport to satisfy the barotropic Sverdrup balance. The lines in Fig. 3a are computed numerically from this solution. Details on this numerical calculation may be found in the code repository linked in the data availability statement.

b. Observed flows at $\delta = 0.01$

At equal layer depths, a complete barotropization occurs when $\delta \xi > 1$ (Fig. 3). When δ is small, however, both the mean flow and the turbulent flow features retain a strong baroclinic signature (Fig. B1). In the lower layer, a Sverdrup flow starts to grow and potential vorticity homogenizes. The upper layer appears to stay in the zonostrophic regime, with strong zonal asymmetry of the turbulent flow features and a complete loss of western intensification. We

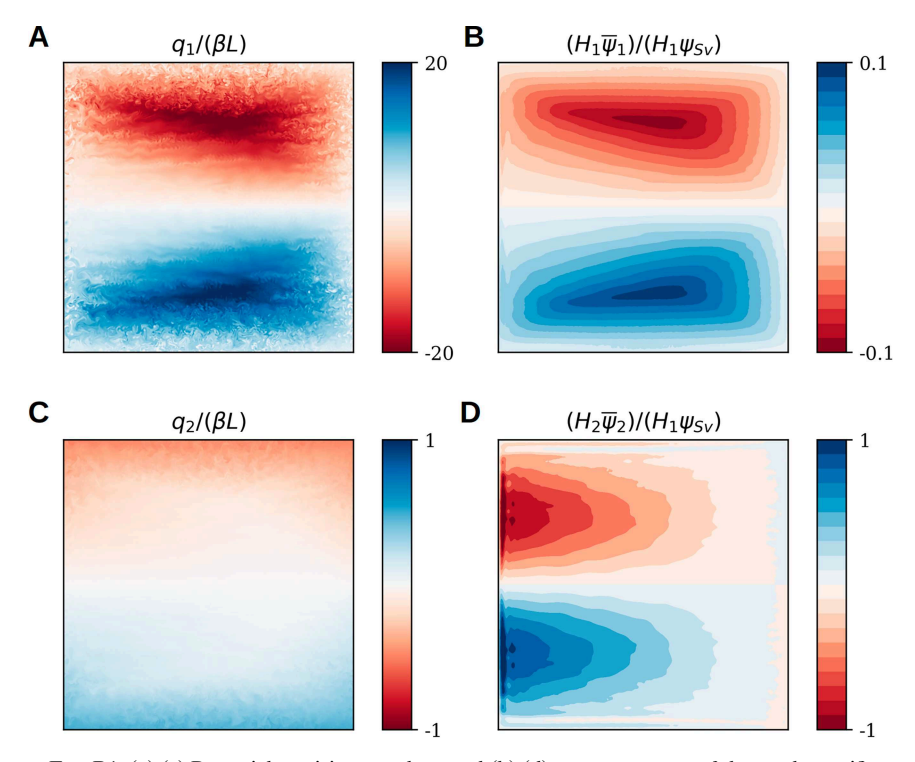


FIG. B1. (a),(c) Potential vorticity snapshots and (b),(d) mean transport of the weak stratification regime low aspect ratio ($\xi = 10^3$, $\delta = 0.01$). Baroclinic activity remains strong even though a Sverdrup flow starts to grow in the lower layer.

discuss here the asymptotic nature of this flow as $\xi \to \infty$. From Eq. (B7), it can be shown that even in the homogenized region, the baroclinic zonal shear leads to a criticality of

$$\frac{u_{\rm bc}}{\beta L_{\rm d}^2} = \frac{1}{\delta},\tag{B8}$$

rationalizing the strong activity of baroclinic instability in the weakly stratified regime when δ is small. Nonetheless, a complete barotropization is expected at larger ξ than those explored here (Fig. 3a), although viscosity might prevent barotropization of turbulence by direct dissipation in the upper layer [Eq. (10)]. Remarkably, potential vorticity homogenization theory works indifferently to the complex dynamics in the upper layer.

APPENDIX C

Instability Calculations

Linearizing the QG equations around a base state with upper-layer velocity only, we obtain

$$\begin{split} \frac{\partial q_1}{\partial t} + J(\psi_1,\,Q_1) + J(\Psi_1,\,q_1) &= \nu \nabla^4 \psi_1, \\ \frac{\partial q_2}{\partial t} + J(\psi_2,\,Q_2) &= \nu \nabla^4 \psi_2. \end{split} \tag{C1}$$

Here, $q_{1/2}$, $\psi_{1/2}$ denote the perturbation fields but are defined as in the main text. The base state is given by

$$Q_1 = \nabla^2 \Psi_1 - \frac{1 - \delta}{L_d^2} \Psi_1 + \beta y, Q_2 = \frac{\delta}{L_d^2} \Psi_1 + \beta y.$$
 (C2)

For the linear stability analysis, three base states were defined. For the interior flow, the base state was given by $\Psi_1 = \pm U_{\rm Sv} y$, where the \pm stands for eastward or westward flow, respectively. In these calculations, ν was set to zero. The problem is governed by two nondimensional numbers, ξ and δ .

The instability analysis of the western boundary layer was carried out by assuming that the problem is invariant in the y direction. The base profile is defined as in Eq. (8) and meant to resemble a double-deck boundary layer structure with an inertial thickness of δ_I and a viscous sublayer δ_P . As in the simulations, the sublayer thickness was set to $\delta_P \approx 3$ km and the inertial layer thickness was set to $\delta_I \approx 72$ km. The explicit dependence on δ_I and δ_P is not explored further.

The instability problem for interior flow is decomposed on Fourier modes and analytically solvable, but the expressions are cumbersome and not very insightful. They can also be found in Pedlosky (1987) and will therefore not be reproduced explicitly, and the reader is referred to Fig. 5 for results. For the western boundary current, decomposition in y is carried out on a Fourier basis, too, and the eigenvectors in x are solved numerically using fourth-order finite-element discretization of the derivatives. Details on this calculation may be found in the code repository linked in the data

availability statement. Again, the results are shown in the main text.

APPENDIX D

Details on the Zonostrophic Regime

To compare jet spacing in the zonostrophic regime with $L_{\rm eff}^{\rm Rh}$, we measured $U_{\rm turb}$ as the average fluctuation speed along the meridional line L/4 < y < 3 L/4, $x = 3\delta_I$, and U_m was measured as the mean transport across the line L/4 < y < 3 L/4, x = L/2 divided by L/2 (Fig. 8a, lines entitled turbulence and staircases, respectively). To determine the number of jets, we calculate the histogram of the potential vorticity along the Hovmöller diagram at midbasin (Fig. 8b). Finally, to obtain the jet spacing, the meridional size over which the histogram was obtained is then divided by the number of distinct peaks that exceed the standard deviation of the histogram, corresponding to the number of distinct homogenized regions.

We performed additional runs with periodic boundary conditions to complement the basin-scale runs. An example simulation can be seen in Fig. D1, where the velocity perturbation is denoted as **u**'. The initial flow fields are given by

$$\psi_1(t=0) = \psi_1' - U_m y , \quad q_1(t=0) = q_1' + \frac{1-\delta}{L_d^2} U_m y, \tag{D1}$$

$$\psi_2(t=0)=0 \; , \;\; q_2(t=0)=-\frac{\delta}{L_+^2}U_m y, \tag{D2} \label{eq:D2}$$

with $q_1' = \nabla^2 \psi_1' - (1 - \delta)/L_d^2(\psi_2' - \psi_1') + \beta y$. The streamfunction was initialized with a randomly generated signal centered

around the wavenumber $1/L_d$, meaning to represent turbulence generated close to the western boundary due to baroclinic instability and then left to freely decay. In all these simulations, the deformation radius was fixed at $L_d=40.7$ km, $U_m=0.2$ m s⁻¹, and $\delta=0.01$ and the domain size was set to L=1523 km. It was also necessary to decrease viscosity to $\nu=0.1$ m² s⁻¹ to obtain final states with clear staircases. This required a numerical resolution of 2048×2048 grid points, and all simulations were run until the mixing of potential vorticity transferred the complete perturbation energy into zonal jets. All other parameters are the same as in the surface-intensified basin-scale simulations (Table 1).

To show the dependence of the jet spacing on the initial perturbation, we carried out five periodic simulations varying the turbulent velocity scale $U_{\rm turb}$. It is defined here as

$$U_{\text{turb}} = \sqrt{\frac{1}{L^2} \int |\nabla \psi_1'|^2 dA}, \tag{D3}$$

at the time of initiation, and was varied between $\beta L_d^2 + U_m$ and $10(\beta L_d^2 + U_m)$. To determine the jet spacing, the histogram of potential vorticity is taken of a snapshot of the final state over the entire domain, and then, the same procedure as for the basin-scale simulations is followed to extract the jet scale.

Figure 8b also shows the slow poleward displacement of the staircases of potential vorticity in the basin-scale runs. Nadiga and Straub (2019) suggested that the displacement speed is correlated with $U_{\rm Sv}$; however, in our simulations, it seemed to match better with the maximum Rossby wave speed βL_d^2 .

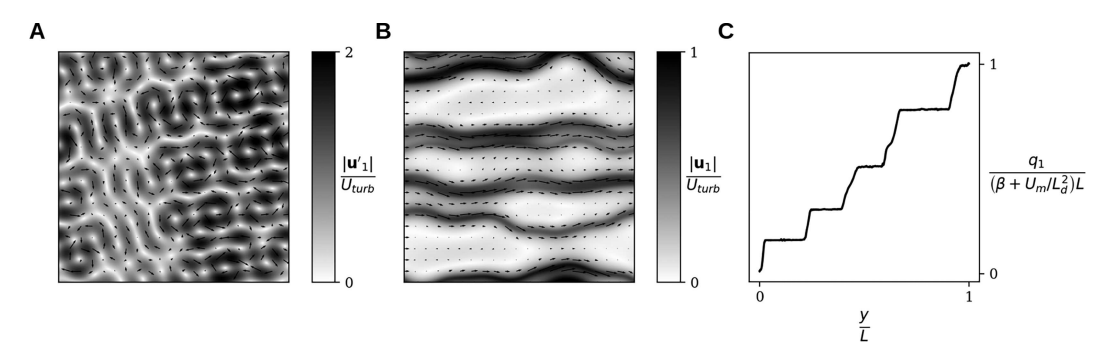


FIG. D1. (a) Initial velocity perturbation, (b) final velocity fields, and (c) meridional profile of potential vorticity for the periodic staircase run at injection velocity $U_{\text{nurb}} = 3.2(\beta L_d^2 + U_m)$.

REFERENCES

- Ajayi, A., J. Le Sommer, E. Chassignet, J.-M. Molines, X. Xu, A. Albert, and E. Cosme, 2020: Spatial and temporal variability of the North Atlantic eddy field from two kilometric-resolution ocean models. *J. Geophys. Res. Oceans*, 125, e2019JC015827, https://doi.org/10.1029/2019JC015827.
- Arbic, B. K., and G. R. Flierl, 2003: Coherent vortices and kinetic energy ribbons in asymptotic, quasi two-dimensional f-plane turbulence. *Phys. Fluids*, **15**, 2177–2189, https://doi.org/10. 1063/1.1582183.
- —, and —, 2004: Effects of mean flow direction on energy, isotropy, and coherence of baroclinically unstable beta-plane geostrophic turbulence. *J. Phys. Oceanogr.*, **34**, 77–93, https://doi.org/10.1175/1520-0485(2004)034<0077:EOMFDO>2.0.
- Berloff, P., I. Kamenkovich, and J. Pedlosky, 2009a: A mechanism of formation of multiple zonal jets in the oceans. *J. Fluid Mech.*, **628**, 395–425, https://doi.org/10.1017/S0022112009006375.
- —, and —, 2009b: A model of multiple zonal jets in the oceans: Dynamical and kinematical analysis. *J. Phys. Oceanogr.*, **39**, 2711–2734, https://doi.org/10.1175/2009JPO4093.1.
- Berloff, P. S., and J. C. McWilliams, 1999a: Large-scale, low-frequency variability in wind-driven ocean gyres. *J. Phys. Oceanogr.*, **29**, 1925–1949, https://doi.org/10.1175/1520-0485(1999)029<1925;LSLFVI>2.0.CO;2.
- —, and —, 1999b: Quasigeostrophic dynamics of the western boundary current. *J. Phys. Oceanogr.*, **29**, 2607–2634, https:// doi.org/10.1175/1520-0485(1999)029<2607:QDOTWB>2.0. CO:2.
- Boland, E. J., A. F. Thompson, E. Shuckburgh, and P. H. Haynes, 2012: The formation of nonzonal jets over sloped topography. *J. Phys. Oceanogr.*, 42, 1635–1651, https://doi.org/10.1175/ JPO-D-11-0152.1.
- Bouchet, F., and A. Venaille, 2012: Statistical mechanics of two-dimensional and geophysical flows. *Phys. Rep.*, **515**, 227–295, https://doi.org/10.1016/j.physrep.2012.02.001.
- Brüggemann, N., and C. Eden, 2015: Routes to dissipation under different dynamical conditions. J. Phys. Oceanogr., 45, 2149– 2168, https://doi.org/10.1175/JPO-D-14-0205.1.
- Burgess, B. H., and D. G. Dritschel, 2022: Potential vorticity fronts and the late-time evolution of large-scale quasi-geostrophic flows. *J. Fluid Mech.*, 939, A40, https://doi.org/10.1017/jfm. 2022.194.
- Charney, J. G., 1955: The gulf stream as an inertial boundary layer. Proc. Natl. Acad. Sci. USA, 41, 731–740, https://doi.org/ 10.1073/pnas.41.10.731.
- Chassignet, E. P., and D. P. Marshall, 2008: Gulf stream separation in numerical ocean models. *Ocean Modeling in an Eddying Regime*, *Geophys. Monogr.*, Vol. 177, Amer. Geophys. Union, 39–61, https://doi.org/10.1029/177GM05.
- —, and X. Xu, 2021: On the importance of high-resolution in large-scale ocean models. *Adv. Atmos. Sci.*, **38**, 1621–1634, https://doi.org/10.1007/s00376-021-0385-7.
- Deremble, B., A. M. Hogg, P. Berloff, and W. K. Dewar, 2011: On the application of no-slip lateral boundary conditions to 'coarsely' resolved ocean models. *Ocean Modell.*, **39**, 411–415, https://doi.org/10.1016/j.ocemod.2011.05.002.
- Dewar, W. K., and A. M. Hogg, 2010: Topographic inviscid dissipation of balanced flow. *Ocean Modell.*, **32** (1–2), 1–13, https://doi.org/10.1016/j.ocemod.2009.03.007.

- Dritschel, D. G., and M. E. McIntyre, 2008: Multiple jets as PV staircases: The Phillips effect and the resilience of eddy-transport barriers. *J. Atmos. Sci.*, **65**, 855–874, https://doi.org/10.1175/2007JAS2227.1.
- —, and R. K. Scott, 2011: Jet sharpening by turbulent mixing. Philos. Trans. Roy. Soc., A369, 754–770, https://doi.org/10. 1098/rsta.2010.0306.
- Flierl, G. R., 1978: Models of vertical structure and the calibration of two-layer models. *Dyn. Atmos. Oceans*, **2**, 341–381, https://doi.org/10.1016/0377-0265(78)90002-7.
- Fox-Kemper, B., 2004: Wind-driven barotropic gyre II: Effects of eddies and low interior viscosity. *J. Mar. Res.*, **62**, 195–232, https://doi.org/10.1357/002224004774201690.
- —, 2005: Reevaluating the roles of eddies in multiple barotropic wind-driven gyres. J. Phys. Oceanogr., 35, 1263–1278, https:// doi.org/10.1175/JPO2743.1.
- —, and J. Pedlosky, 2004: Wind-driven barotropic gyre I: Circulation control by eddy vorticity fluxes to an enhanced removal region. *J. Mar. Res.*, **62**, 169–193, https://doi.org/10.1357/002224004774201681.
- Frishman, A., J. Laurie, and G. Falkovich, 2017: Jets or vortices—What flows are generated by an inverse turbulent cascade? *Phys. Rev. Fluids*, **2**, 032602, https://doi.org/10.1103/PhysRevFluids.2.032602.
- Fu, L.-L., and G. R. Flierl, 1980: Nonlinear energy and enstrophy transfers in a realistically stratified ocean. *Dyn. Atmos. Oceans*, 4, 219–246, https://doi.org/10.1016/0377-0265(80) 90029-9.
- Gallet, B., and R. Ferrari, 2021: A quantitative scaling theory for meridional heat transport in planetary atmospheres and oceans. AGU Adv., 2, e2020AV000362, https://doi.org/10. 1029/2020AV000362.
- Greatbatch, R. J., and B. T. Nadiga, 2000: Four-gyre circulation in a barotropic model with double-gyre wind forcing. *J. Phys. Oceanogr.*, **30**, 1461–1471, https://doi.org/10.1175/1520-0485 (2000)030<1461:FGCIAB>2.0.CO;2.
- —, X. Zhai, J.-D. Kohlmann, and L. Czeschel, 2010: Ocean eddy momentum fluxes at the latitudes of the Gulf Stream and the Kuroshio extensions as revealed by satellite data. *Ocean Dyn.*, 60, 617–628, https://doi.org/10.1007/s10236-010-0282-6
- Grooms, I., L.-P. Nadeau, and K. S. Smith, 2013: Mesoscale eddy energy locality in an idealized ocean model. *J. Phys. Ocean*ogr., 43, 1911–1923, https://doi.org/10.1175/JPO-D-13-036.1.
- Haidvogel, D. B., J. C. McWilliams, and P. R. Gent, 1992: Boundary current separation in a quasigeostrophic, eddy-resolving ocean circulation model. J. Phys. Oceanogr., 22, 882–902, https://doi.org/10.1175/1520-0485(1992)022<0882:BCSIAQ>2. 0.CO:2.
- Held, I. M., and V. D. Larichev, 1996: A scaling theory for horizontally homogeneous, baroclinically unstable flow on a beta plane. *J. Atmos. Sci.*, **53**, 946–952, https://doi.org/10.1175/1520-0469(1996)053<0946:ASTFHH>2.0.CO;2.
- Holland, W. R., 1978: The role of mesoscale eddies in the general circulation of the ocean—Numerical experiments using a wind-driven quasi-geostrophic model. *J. Phys. Oceanogr.*, 8, 363–392, https://doi.org/10.1175/1520-0485(1978)008<0363: TROMEI>2.0.CO;2.
- Ierley, G. R., and O. G. Ruehr, 1986: Analytic and numerical solutions of a nonlinear boundary-layer problem. *Stud. Appl. Math.*, 75 (1), 1–36, https://doi.org/10.1002/sapm19867511.

- —, and W. R. Young, 1988: Inertial recirculation in a *β*-plane corner. *J. Phys. Oceanogr.*, **18**, 683–689, https://doi.org/10. 1175/1520-0485(1988)018<0683:IRIAPC>2.0.CO;2.
- —, and —, 1991: Viscous instabilities in the western boundary layer. *J. Phys. Oceanogr.*, **21**, 1323–1332, https://doi.org/10.1175/1520-0485(1991)021<1323:VIITWB>2.0.CO;2.
- Jansen, M., and R. Ferrari, 2012: Macroturbulent equilibration in a thermally forced primitive equation system. *J. Atmos. Sci.*, 69, 695–713, https://doi.org/10.1175/JAS-D-11-041.1.
- Kukharkin, N., S. A. Orszag, and V. Yakhot, 1995: Quasicrystallization of vortices in drift-wave turbulence. *Phys. Rev. Lett.*, 75, 2486–2489, https://doi.org/10.1103/PhysRevLett.75.2486.
- Kurashina, R., P. Berloff, and I. Shevchenko, 2021: Western boundary layer nonlinear control of the oceanic gyres. *J. Fluid Mech.*, **918**, A43, https://doi.org/10.1017/jfm.2021.384.
- Marshall, D., and J. Marshall, 1992: Zonal penetration scale of midlatitude oceanic jets. *J. Phys. Oceanogr.*, **22**, 1018–1032, https://doi.org/10.1175/1520-0485(1992)022<1018:ZPSOMO>2. 0.CO:2.
- Meunier, J., B. Miquel, and B. Gallet, 2023: Vertical structure of buoyancy transport by ocean baroclinic turbulence. *Geophys. Res. Lett.*, 50, e2023GL103948, https://doi.org/10.1029/2023GL 103948.
- Miller, L., B. Deremble, and A. Venaille, 2024: Gyre turbulence: Anomalous dissipation in a two-dimensional ocean model. *Phys. Rev. Fluids*, 9, L051801, https://doi.org/10.1103/PhysRev Fluids,9.L051801.
- Nadiga, B. T., and D. N. Straub, 2010: Alternating zonal jets and energy fluxes in barotropic wind-driven gyres. *Ocean Modell.*, 33, 257–269, https://doi.org/10.1016/j.ocemod.2010.02.007.
- —, and —, 2019: Meridional propagation of zonal jets in ocean gyres. Zonal Jets: Phenomenology, Genesis, and Physics, B. Galperin, and P. L. Read, Eds., Cambridge University Press, 284–291.
- Nasser, A.-A., G. Madec, C. de Lavergne, L. Debreu, F. Lemarié, and E. Blayo, 2023: Sliding or stumbling on the staircase: Numerics of ocean circulation along piecewise-constant coastlines. J. Adv. Model. Earth Syst, 15, e2022MS003594, https:// doi.org/10.1029/2022MS003594.
- Nikurashin, M., G. K. Vallis, and A. Adcroft, 2013: Routes to energy dissipation for geostrophic flows in the Southern Ocean. *Nat. Geosci.*, **6**, 48–51, https://doi.org/10.1038/ngeo1657.
- Pedlosky, J., 1987: Geophysical Fluid Dynamics. Springer, 724 pp. Rhines, P. B., 1975: Waves and turbulence on a beta-plane. J. Fluid Mech., 69, 417–443, https://doi.org/10.1017/S0022112 075001504
- —, and W. R. Young, 1982: Homogenization of potential vorticity in planetary gyres. *J. Fluid Mech.*, **122**, 347–367, https://doi.org/10.1017/S0022112082002250.
- Salmon, R., 1998: Lectures on Geophysical Fluid Dynamics. Oxford University Press, 400 pp.

- Sánchez-Román, A., F. Gues, R. Bourdalle-Badie, M.-I. Pujol, A. Pascual, and M. Drévillon, 2024: Changes in the Gulf Stream path over the last 3 decades. Copernicus Ocean State Rep. 4-osr8, 4 pp., https://doi.org/10.5194/sp-4-osr8-4-2024.
- Scott, R. B., and D. N. Straub, 1998: Small viscosity behavior of a homogeneous, quasi-geostrophic, ocean circulation model. J. Mar. Res., 56, 1225–1258, https://doi.org/10.1357/002224098 765093625.
- Sheremet, V., V. Kamenkovich, and A. Pastushkov, 1995: Analysis of the barotropic model of the subtropical gyre in the ocean for finite Reynolds numbers. Part II. J. Mar Res., 53, 995–1024, https://doi.org/10.1357/0022240953212945.
- Simonnet, E., 2005: Quantization of the low-frequency variability of the double-gyre circulation. *J. Phys. Oceanogr.*, **35**, 2268–2290, https://doi.org/10.1175/JPO2806.1.
- Smith, K. S., and G. K. Vallis, 2001: The scales and equilibration of midocean eddies: Freely evolving flow. J. Phys. Oceanogr., 31, 554–571, https://doi.org/10.1175/1520-0485(2001)031<0554: TSAEOM>2.0.CO:2.
- Spall, M., 2000: Generation of strong mesoscale eddies by weak ocean gyres. J. Mar. Res., 58, 97–116, https://doi.org/10.1357/ 002224000321511214.
- Stone, P. H., 1978: Baroclinic adjustment. *J. Atmos. Sci.*, **35**, 561–571, https://doi.org/10.1175/1520-0469(1978)035<0561: BA>2.0.CO;2.
- Sun, S., L. Wu, and B. Qiu, 2013: Response of the inertial recirculation to intensified stratification in a two-layer quasigeostrophic ocean circulation model. *J. Phys. Oceanogr.*, 43, 1254–1269, https://doi.org/10.1175/JPO-D-12-0111.1.
- Uchida, T., and Coauthors, 2022: Cloud-based framework for inter-comparing submesoscale-permitting realistic ocean models. *Geosci. Model Dev.*, 15, 5829–5856, https://doi.org/ 10.5194/gmd-15-5829-2022.
- Vallis, G. K., 2017: Atmospheric and Oceanic Fluid Dynamics. Cambridge University Press, 964 pp.
- Venaille, A., and F. Bouchet, 2011: Oceanic rings and jets as statistical equilibrium states. J. Phys. Oceanogr., 41, 1860–1873, https://doi.org/10.1175/2011JPO4583.1.
- —, L.-P. Nadeau, and G. Vallis, 2014: Ribbon turbulence. *Phys. Fluids*, **26**, 126605, https://doi.org/10.1063/1.4904878.
- —, T. Dauxois, and S. Ruffo, 2015: Violent relaxation in two-dimensional flows with varying interaction range. *Phys. Rev. E*, 92, 011001, https://doi.org/10.1103/PhysRevE.92.011001.
- Veronis, G., 1966: Wind-driven ocean circulation—Part 2. Numerical solutions of the non-linear problem. *Deep-Sea. Res. Oceanogr. Abstr.*, **13**, 31–55, https://doi.org/10.1016/0011-7471(66) 90004-0.
- Wardle, R., and J. Marshall, 2000: Representation of eddies in primitive equation models by a PV flux. *J. Phys. Oceanogr.*, **30**, 2481–2503, https://doi.org/10.1175/1520-0485(2000)030< 2481:ROEIPE>2.0.CO;2.